Image reconstruction from finite numbers of projections

1973 J. Phys. A: Math. Nucl. Gen. 6 361

(http://iopscience.iop.org/0301-0015/6/3/011)

J. Phys. A: Math., Nucl. Gen., Vol. 6, March 1973. Printed in Great Britain.

Image reconstruction from finite numbers of projections

P R Smith†, T M Peters‡ and R H T Bates‡
University of Canterbury, Christchurch, New Zealand

MS received 18 July 1972

Abstract. Several results are obtained appertaining to the reconstruction of a two-dimensional image from a finite number of projections. Several schemes are considered for interpolating between the given data. When a trigonometrical Fourier series is used for angular interpolation then one finds, firstly, a consistency condition whereby *a posteriori* estimates can be made of the errors in the given data and, secondly, a basic image which contains only that information common to all physically permissible interpolation schemes. This basic image is necessarily free of misleading artefacts but it is computationally slow. Several computationally rapid interpolation schemes (based on the fast Fourier transform algorithm) are found to give good quality images, provided the given number of projections is sufficient to resolve the major details of the true image. Computational examples are presented for ideal data and for x ray projections of a bovine shin bone. The significance of the results for general scientific work and for clinical radiography is indicated. It is pointed out that it is dangerous to make *a priori* assumptions concerning the topological structure of the image, and a computational example is presented showing that a contrived image can be accurately reconstructed from a single projection.

1. Introduction

In many sciences there is currently interest in reconstructing images from projections. Molecular biological structure is deduced from electron micrographs (cf DeRosier and Klug 1968, Crowther *et al* 1970b, Vainshtein 1971, Klug and Crowther 1972). In radio astronomy, brightness temperature maps of the celestial sphere are produced from interferograms (cf Bracewell 1961, Swenson and Mathur 1968, Bates and Napier 1972). In medical tomography, the interiors of bodies are imaged from radiographic projections (cf Stanton 1969, Bates and Peters 1971). In engineering, x rays are used for nondestructive testing of fabricated parts (cf Schneeman 1968).

The images can be formed either by direct manipulation of the projections (cf Bracewell and Riddle 1967, Gordon *et al* 1970, Crowther *et al* 1970a, Ramachandran and Lakshminarayanan 1971, Gilbert 1972a) or by making intermediate use of Fourier transforms (Bracewell 1956, DeRosier and Klug 1968, Crowther *et al* 1970a). We are concerned with the latter, when only a finite number of projections is available, so that interpolation between the given data is required. We note that the basic theory (based on the Whittaker–Nyquist–Shannon–Woodward sampling theorem) of interpolating between projections has been given by Crowther *et al* (1970a). We repeat none of their work here.

† Department of Physics. Present address: Biozentrum der Universität Basel, CH-4056 Basel, Switzerland.
‡ Department of Electrical Engineering.

By extending an analysis due to Cormack (1963, 1964) we derive a consistency condition which permits *a posteriori* assessment of the errors in given data. We show that there exists a basic image which contains only that information common to all physically permissible interpolations of a particular set of given data.

Considerable computer time is required for rigorously established methods of reconstructing images, such as the method of Crowther *et al* (1970a) and our method of reconstructing the basic image. We examine a number of straightforward methods of interpolating between given projections. We find that, provided we do not attempt to reconstruct detail finer than that allowed by the given number of projections, there are only minor differences between the images reconstructed using several different interpolation schemes. We conclude from this that the simplest of the schemes will usually provide a satisfactory image. This is discussed further in §§ 8 and 9.

In § 2 we give the necessary background. The restrictions imposed by a finite number of given projections are set down in § 3. Several interpolation schemes are introduced in § 4. The consistency condition is developed in § 5. The theory of the basic image is given in § 6.

There has been controversy over what is meant by resolution in reconstructed images (Crowther and Klug 1971, Bellman *et al* 1971). With Klug and Crowther (1972) we feel that considerable difficulty is caused by resolution being (unavoidably) a somewhat loose concept. In § 7 we use the basic image to define the detail which can be unambiguously reconstructed from a given number of projections. We also give quantitative estimates of the 'clutter' (a descriptive term borrowed from radar, cf Skolnik (1962)) introduced into the image by simple interpolation schemes when the number of projections is finite. We also show that one must be careful not to make unnecessary *a priori* assumptions concerning the information structure of the image. To emphasize this we show that, by extension of the recently introduced method ART (Gordon *et al* 1970, Herman and Rowland 1971) certain images can be reconstructed perfectly, in principle, from a single projection.

In § 8 we present a number of computational examples to demonstrate the various points made here. We use both ideal data and measured x ray projections of a bovine shin bone obtained from standard clinical radiographic apparatus. In § 9 we discuss the significance of our results and outline several computational considerations. We emphasize the value of the fast Fourier transform algorithm (cf Bergland 1969).

2. Radiation transforms

We state here those Fourier transform relations (previously given the descriptive name *radiation transforms* (Bates and Peters 1971)) which connect a density distribution with its projections (or 'shadowgrams' as they are sometimes called). The theory is known (cf Bracewell 1956, Bates and Peters 1971) so that no derivations are included. It must be remembered that in any particular situation the actual 'density' to which the theory refers depends upon the type of radiation used and the type of body being irradiated.

We denote the two-dimensional density by $\omega(x, y)$ in cartesian coordinates and $\lambda(r, \theta)$ in polar coordinates (figure 1). We denote by μ the mass associated with the density:

$$\mu = \int\int_{-\infty}^{\infty} \omega(x, y)\,\mathrm{d}x\,\mathrm{d}y = \int\int_{-\infty}^{\infty} \omega(x, y)\,\mathrm{d}\xi\,\mathrm{d}\eta = \int_0^a \int_0^{2\pi} \lambda(r, \theta) r\,\mathrm{d}\theta\,\mathrm{d}r \tag{2.1}$$

where the infinite limits in the first two double integrals imply that μ is the total mass.

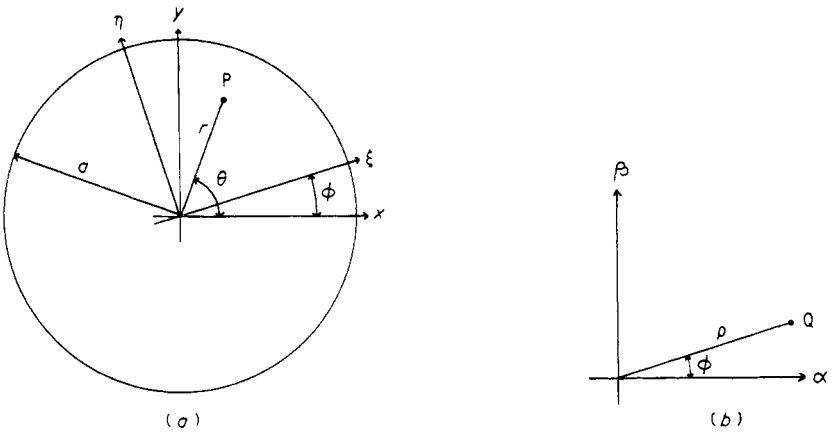

Figure 1. Coordinate systems. (*a*) Real plane. Coordinates of arbitrary point P: (x, y) cartesian, (r, θ) polar. The coordinates (ξ, η) are cartesian inclined at an angle to (x, y). The density is assumed zero for $r > a$. (*b*) Fourier transform plane. Coordinates of arbitrary point Q: (α, β) cartesian, (ρ, ϕ) polar.

The finite radial limit in the third integral indicates that we normalize the sizes of the bodies we study by requiring that all their densities are contained within circumscribing circles of radius a (figure 1).

The radiation passes through a particular cross section of the body in parallel, straight lines. The variation of density throughout this cross section is $\omega(x, y)$. The intensity of each ray of the radiation, having passed through the cross section, is attenuated by a factor dependent upon the integrated density along the ray. It is from sets of measured values of this attenuation that an image of the cross section is reconstructed. It is perhaps worth noting that, whereas images formed by wave fields are usually in planes perpendicular to radiation beams, in this case the image is parallel to the radiation beam.

For a particular value of ϕ, we call the integrated density, along lines perpendicular to the ξ axis, a projection and we denote it by $f(\xi, \phi)$. We call the set of all projections, for $0 \leqslant \phi \leqslant \pi$, the projected density. So, in terms of the density, $f(\xi, \phi)$ is given by

$$f(\xi, \phi) = \int_{-\infty}^{\infty} \omega(x, y)\, \mathrm{d}\eta = \int_{-\infty}^{\infty} \lambda(r, \theta)\, \mathrm{d}\eta. \tag{2.2}$$

An actual physical measurement seldom provides a projection directly. However, the reduction of measured data to projections has been described (cf Vogt *et al* 1969). Note, from equation (2.1), that

$$\int_{-\infty}^{\infty} f(\xi, \phi)\, \mathrm{d}\xi = \mu. \tag{2.3}$$

We denote the two-dimensional Fourier transform of the density by $\Omega(\alpha, \beta)$ in cartesian coordinates and $\Lambda(\rho, \phi)$ in polar coordinates (figure 1), where

$$\begin{aligned}\Omega(\alpha, \beta) = \Lambda(\rho, \phi) &= \int\int_{-\infty}^{\infty} \omega(x, y) \exp\{\mathrm{i}2\pi(\alpha x + \beta y)\}\, \mathrm{d}x\, \mathrm{d}y \\ &= \int_0^a \int_0^{2\pi} \lambda(r, \theta) \exp\{\mathrm{i}2\pi\rho r \cos(\phi - \theta)\} r\, \mathrm{d}\theta\, \mathrm{d}r.\end{aligned} \tag{2.4}$$

We call the integral of all rays passing through the point P of figure 1 the layergram (a more appropriate term, we feel, than back projection as Gilbert (1972a) has called it) which we denote by $g(r, \theta)$, where

$$g(r, \theta) = \int_0^{\pi} f(r\cos(\theta - \phi), \phi)\, d\phi. \tag{2.5}$$

Note that, for any particular ξ, the interval $0 \leqslant \phi \leqslant \pi$ spans all different $f(\xi, \phi)$. Also note that even though $f(\xi, \phi) = 0$ for $|\xi| > a$, $g(r, \phi)$ has value for all finite r, because however large r is there is always a range of values of ϕ such that $|r\cos(\theta - \phi)| \leqslant a$.

We use $\mathcal{F}_{(n)}\{\cdot\}$ to denote an n-dimensional Fourier transform from the real plane to the transform plane (figure 1). We use $\mathcal{F}_{(n)}^{-1}\{\cdot\}$ to denote an inverse n-dimensional transform. For one-dimensional transforms it is necessary to indicate the variable with respect to which the transform is taken (ie which variable becomes the variable of integration in the Fourier integral). This is done for a variable ξ by writing $\mathcal{F}_{(1)\xi}\{\cdot\}$.

There are two basic radiation transform formulae. The first is

$$\Lambda(\rho, \phi) = \mathcal{F}_{(1)\xi}\{f(\xi, \phi)\} \tag{2.6}$$

which means that if all projections are one-dimensionally transformed, the complete Fourier transform of the density is obtained. The second formula is

$$\Lambda(\rho, \phi) = \rho\mathcal{F}_{(2)}\{g(r, \theta)\} \tag{2.7}$$

which we (Bates and Peters 1971) have noted as being an appropriate basis for optical reconstructions of the density. The density itself is given by the two formulae:

$$\omega(x, y) = \lambda(r, \theta) = \mathcal{F}_{(2)}^{-1}\{\mathcal{F}_{(1)\xi}\{f(\xi, \phi)\}\} \tag{2.8}$$

$$\omega(x, y) = \lambda(r, \theta) = \mathcal{F}_{(2)}^{-1}\{\rho\mathcal{F}_{(2)}\{g(r, \theta)\}\}. \tag{2.9}$$

It is worth noting that

$$\frac{1}{\rho} = \mathcal{F}_{(2)}\left\{\frac{1}{r}\right\} \tag{2.10}$$

which implies that the convolution (denoted by *) theorem gives

$$g(r, \theta) = \frac{1}{r} * \lambda(r, \theta) \tag{2.11}$$

as an alternative form of (2.9). Some 'direct' methods (Bracewell and Riddle 1967, Ramachandran and Lakshminarayanan 1971) of inferring the density from projections are based on (2.11). However, computations based on (2.9) are necessarily much faster when it is required to compute the density at a large number of points, because (2.11) cannot take advantage of the fast Fourier transform algorithm (Bergland 1969). We introduce here the term rho-filtered layergram for the right hand side of (2.9), because the factor ρ can be realized readily in an optical filter (cf Goodman 1968). This has suggested to us a possible application in clinical radiography. Presently available transverse tomographic apparatus gives an image which is a distorted form of layergram (cf Stanton 1969, Kishi *et al* 1969, Kotoulas and Sinis 1970). Now, layergrams are heavily blurred representations of actual densities (Bates and Peters 1971, Gilbert 1972a). Consequently, we have proposed that suitably modified tomographic apparatus could produce undistorted layergrams, from which accurate densities could be obtained after rho filtering in a standard optical bench (Bates and Peters 1971).

3. Consequences of finite number of projections

We are concerned with reconstructing the density from a finite number N of projections. So, we are given $f(\xi, \phi)$ for a finite set $\{\phi_n | 1 \leqslant n \leqslant N\}$ of values of ϕ. Often we only get $f(\xi, \phi_n)$ at discrete values of ξ, but since there is rarely any technical problem in sampling extremely closely in ξ, we assume that $f(\xi, \phi_n)$ is given effectively continuously in ξ.

Our restricted knowledge of the projected density means that all we can compute from (2.5) is the discrete layergram

$$g_N(r, \theta) = \frac{\pi}{N} \sum_{n=1}^{N} f(r\cos(\theta - \phi_n), \phi_n). \tag{3.1}$$

We introduce the star function

$$\text{star}_N(r, \theta) = \frac{2\pi}{Nr} \sum_{n=1}^{N} \{\delta(\theta - \phi_n) + \delta(\theta - \phi_n - \pi)\} \tag{3.2}$$

where $\delta(\cdot)$ denotes the Dirac delta function. Note that

$$\text{star}_N(\rho, \phi + \tfrac{1}{2}\pi) = \mathscr{F}_{(2)}\{\text{star}_N(r, \theta)\}. \tag{3.3}$$

All that we can compute from (2.6) of the Fourier transform of the density is

$$\Lambda_N(\rho, \phi) = \Lambda(\rho, \phi)\, \text{star}_N(\rho, \phi). \tag{3.4}$$

It is convenient to introduce a modified projected density $F(\xi, \phi)$ defined by

$$\left.\begin{aligned} F(\xi, \phi) &= f(\xi, \phi), & \xi \geqslant 0 \\ F(-\xi, \phi + \pi) &= f(\xi, \phi), & \xi \leqslant 0 \end{aligned}\right\} 0 \leqslant \phi \leqslant \pi \tag{3.5}$$

which implies that $F(\xi, \phi)$ exists in $0 \leqslant \xi \leqslant a, 0 \leqslant \phi < 2\pi$ whereas $f(\xi, \phi)$ exists in $-a \leqslant \xi \leqslant a, 0 \leqslant \phi < \pi$. If we denote by $f_N(\xi, \phi)$ and $F_N(\xi, \phi)$ the parts we know of the projected densities then

$$F_N(\xi, \phi) = F(\xi, \phi)\, \text{star}_N(\xi, \phi) = \left.\begin{aligned} f_N(\xi, \phi), &\qquad \phi_1 \leqslant \phi \leqslant \phi_N \\ f_N(-\xi, \phi), &\qquad \phi_1 + \pi \leqslant \phi \leqslant \phi_N + \pi \end{aligned}\right\} \xi \geqslant 0. \tag{3.6}$$

We can attempt to estimate $f(\xi, \phi)$ and $F(\xi, \phi)$ for values of ϕ not belonging to $\{\phi_n\}$ by interpolating between the given data. We use $\bar{f}_N(\xi, \phi)$ and $\bar{F}_N(\xi, \phi)$ to denote such estimates obtained from any of the interpolation schemes listed in the next section, when N projections are originally provided. We use $\bar{\lambda}_N(r, \theta)$, $\bar{g}_N(r, \theta)$ and $\bar{\Lambda}_N(\rho, \phi)$ to denote the density, the layergram and the Fourier transform of the density computed from any of the interpolation schemes.

We need two operations, spread_N and lin_N, to describe certain of the interpolation schemes introduced in the next section. For a function $H(r, \theta)$ defined only on the arms of $\text{star}_N(r, \theta)$:

$$\text{spread}_N\{H(r, \theta)\} = H(r, \theta_n), \qquad \frac{\theta_n - \theta_{n-1}}{2} \leqslant \theta < \frac{\theta_{n+1} - \theta_n}{2} \tag{3.7}$$

$$\text{lin}_N\{H(r, \theta)\} = \frac{(\theta - \theta_n)H(r, \theta_{n+1}) + (\theta_{n+1} - \theta)H(r, \theta_n)}{\theta_{n+1} - \theta_n}, \qquad \theta_n \leqslant \theta < \theta_{n+1}. \tag{3.8}$$

4. Interpolation schemes

The following interpolation schemes are arranged in order of increasing computational complexity.

4.1. Discrete layergram

$$\bar{\lambda}_N(r, \theta) = g_N(r, \theta) \tag{4.1}$$

which is the crudest available estimate of the density. It has the advantage of being computable direct from the given projections, without interpolation. It is of interest since it represents the idealized output of conventional medical x ray tomographs (cf Bates and Peters 1971).

4.2. Rho-filtered discrete layergram

$$\bar{\lambda}_N(r, \theta) = \mathscr{F}_{(2)}^{-1}\{\rho \Lambda_N(\rho, \phi)\} \tag{4.2}$$

which is the estimate of the density provided by (2.9) when no explicit interpolation is used. This is equivalent to Gilbert's (1972a) 'corrected back projection'.

4.3. Spread interpolation

$$\bar{\lambda}_N(r, \theta) = \mathscr{F}_{(2)}^{-1}\{\text{spread}_N\{\Lambda_N(\rho, \phi + \tfrac{1}{2}\pi)\}\} \tag{4.3}$$

which is the simplest interpolation scheme that can be applied in the Fourier transform plane.

4.4. Linear interpolation

$$\bar{\lambda}_N(r, \theta) = \mathscr{F}_{(2)}^{-1}\{\text{lin}_N\{\Lambda_N(\rho, \phi + \tfrac{1}{2}\pi)\}\} \tag{4.4}$$

which is another simple interpolation scheme applied in the Fourier transform plane.

4.5. Fourier series interpolation (FSI)

The given $F_N(\xi, \phi)$ is interpolated by

$$\bar{F}_N(\xi, \phi) = \sum_{m=0}^{N} A_m(\xi) \cos(m\phi) + \sum_{m=1}^{N-1} B_m(\xi) \sin(m\phi) \tag{4.5}$$

where the $A_m(\xi)$ and $B_m(\xi)$, which are computed in standard fashion (cf Hildebrand 1956), are such that

$$\left.\begin{aligned} \bar{F}_N(\xi, \phi_n) &= F_N(\xi, \phi_n) \\ \bar{F}_N(\xi, \phi_n + \pi) &= F_N(\xi, \phi_n + \pi) \end{aligned}\right\} 1 \leqslant n \leqslant N. \tag{4.6}$$

Within $0 \leqslant \xi \leqslant a$, by definition the interval containing all the projected density, we define

$$\begin{matrix} A_{2m}(\xi) \\ B_{2m}(\xi) \end{matrix} = \sum_{p=0}^{L} \begin{matrix} \alpha_{2m,p} \\ \beta_{2m,p} \end{matrix} \cos\{(2p+1) \arcsin(\xi/a)\} \tag{4.7}$$

$$\begin{matrix} A_{2m+1}(\xi) \\ B_{2m+1}(\xi) \end{matrix} = \sum_{p=1}^{L} \begin{matrix} \alpha_{2m+1,p} \\ \beta_{2m+1,p} \end{matrix} \sin\{2p \arcsin(\xi/a)\} \tag{4.8}$$

where the integer L is large enough to include all computationally significant $\alpha_{m,p}$ and

$\beta_{m,p}$, which are computed in standard fashion (cf Hildebrand 1956) from the known $A_m(\xi)$ and $B_m(\xi)$, since the sets $\{\cos\{(2p+1)\arcsin(\xi/a)\}|0 \leqslant p < \infty\}$ and $\{\sin\{2p \arcsin(\xi/a)\}|1 \leqslant p < \infty\}$ are orthogonal in $0 \leqslant \xi \leqslant a$. We note here that it is advantageous to sample the projected density at equal increments in arc sin (ξ/a) in order to simplify the computation of the $\alpha_{m,p}$ and $\beta_{m,p}$. We now define

$$\begin{aligned} N_1 &= \tfrac{1}{2}N, && N \text{ even} \\ &= \tfrac{1}{2}(N-1), && N \text{ odd} \end{aligned} \tag{4.9}$$

$$\begin{aligned} N_2 &= \tfrac{1}{2}(N-2), && N \text{ even} \\ &= \tfrac{1}{2}(N-1), && N \text{ odd} \end{aligned} \tag{4.10}$$

$$\begin{aligned} \Delta_n^{(1)} &= 0, && n = N_2, && N \text{ odd} \\ &= 1, && n \neq N_2, && N \text{ odd} \\ &= 1, && N \text{ even} \end{aligned} \tag{4.11}$$

$$\begin{aligned} \Delta_n^{(2)} &= 0, && n = 0 \\ &= 1, && 1 \leqslant n \leqslant N_1 - 1 \\ &= 0, && n = N_1, && N \text{ even} \\ &= 1, && n = N_1, && N \text{ odd.} \end{aligned} \tag{4.12}$$

From (3.6) and (4.6) the interpolated projected density $\bar{f}_N(\xi, \phi)$ can be written as

$$\begin{aligned} \bar{f}_N(\xi, \phi) &= \bar{F}_N(\xi, \phi), && \xi \geqslant 0 \\ &= \bar{F}_N(-\xi, \phi + \pi), && \xi < 0 \end{aligned} \tag{4.13}$$

which we substitute for $f(\xi, \phi)$ in (2.6), obtaining with the use of (4.5) the estimate

$$\begin{aligned} \bar{\Lambda}_N(\rho, \phi) = 2 &\sum_{m=0}^{N_1} \cos(2m\phi) \int_0^a A_{2m}(\xi) \cos(2\pi\rho\xi) \mathrm{d}\xi \\ &+ \mathrm{i}2 \sum_{m=0}^{N_2} \cos\{(2m+1)\phi\} \int_0^a A_{2m+1}(\xi) \sin(2\pi\rho\xi)\, \mathrm{d}\xi \\ &+ 2 \sum_{m=0}^{N_2} \sin(2m\phi) \int_0^a B_{2m}(\xi) \cos(2\pi\rho\xi)\, \mathrm{d}\xi \\ &+ \mathrm{i}2 \sum_{m=0}^{N_2} \Delta_m^{(1)} \sin\{(2m+1)\phi\} \int_0^a B_{2m+1}(\xi) \sin(2\pi\rho\xi)\, \mathrm{d}\xi \end{aligned} \tag{4.14}$$

for the Fourier transform of the density. Substituting (4.7) and (4.8) into (4.14), and using the Fourier inverses of formulae 11.4.35 and 11.4.36 of Abramowitz and Stegun (1965), gives

$$\begin{aligned} \bar{\Lambda}_N(\rho, \phi) = \sum_{p=0}^{L} \Bigg(&(p+\tfrac{1}{2}) \sum_{m=0}^{N_1} \{\alpha_{2m,p} \cos(2m\phi) + \Delta_m^{(2)} \beta_{2m,p} \sin(2m\phi)\} \frac{\mathrm{J}_{2p+1}(2\pi a\rho)}{\rho} \\ &+ \mathrm{i}p\Delta_p^{(2)} \sum_{m=0}^{N_2} [\alpha_{2m+1,p} \cos\{(2m+1)\phi\} \\ &+ \Delta_m^{(1)} \beta_{2m+1,p} \sin\{(2m+1)\phi\}] \frac{\mathrm{J}_{2p}(2\pi a\rho)}{\rho} \Bigg) \end{aligned} \tag{4.15}$$

where $J_m(\cdot)$ denotes the Bessel function of the first kind of order m. The estimated density $\bar{\lambda}_N(r, \theta)$ is the inverse Fourier transform of $\bar{\Lambda}_N(\rho, \phi)$. This is conveniently evaluated by first expressing the kernel of the Fourier integral as a trigonometrical Fourier series (cf formulae 9.1.44 and 9.1.45 of Abramowitz and Stegun (1965)). It then follows (formulae 11.4.33 and 11.4.34 of Ambramowitz and Stegun (1965)) that

$$\begin{aligned}\bar{\lambda}_N(r,\theta) = \sum_{p=0}^{L}\Bigg\{&\frac{2p+1}{2a}\sum_{m=M_1^-}^{M_1^+}\{\alpha_{2m,p}\cos(2m\theta)+\Delta_m^{(2)}\beta_{2m,p}\sin(2m\theta)\}H_{m,p}\left(\frac{r}{a}\right)\\&+\mathrm{i}\frac{p}{r}\Delta_p^{(2)}\sum_{m=M_2^-}^{M_2^+}[\alpha_{2m+1,p}\cos\{(2m+1)\theta\}\\&+\Delta_m^{(1)}\beta_{2m+1,p}\sin\{(2m+1)\theta\}]H_{p,m}\left(\frac{a}{r}\right)\Bigg\}\end{aligned}\tag{4.16}$$

$$\begin{aligned}H_{m,p}(x) &= \int_0^\infty J_{2m}(xt)J_{2p+1}(t)\,\mathrm{d}t\\&= \frac{(m+p)!x^{2m}}{(2m)!\Gamma(p-m+1)}{}_2F_1(m+p+1, m-p; 2m+1; x^2), \qquad x<1\\&= \frac{(m+p)!x^{-2(p+1)}}{(2p+1)!\Gamma(m-p)}{}_2F_1(m+p+1, p-m+1; 2p+2; x^{-2}), \qquad x>1\end{aligned}\tag{4.17}$$

where $\Gamma(\cdot)$ and ${}_2F_1(\cdot)$ denote the gamma and hypergeometric functions respectively. The limits on the inner summations in (4.16) are represented by special symbols in order to clarify the exposition of §§ 5 and 6. They have the values

$$M_1^- = 0, \qquad M_1^+ = N_1, \qquad M_2^- = 0, \qquad M_2^+ = N_2. \tag{4.18}$$

This interpolation scheme is much more complicated than the previous ones. It also requires more computation time. However, it is of considerable theoretical interest, as is shown in §§ 5 and 6. This is why it has been described in detail here. The previous analysis by Cormack (1963, 1964) does not cover the points which we must accentuate.

5. Consistency condition

The hypergeometric functions in (4.17) are well behaved for all m and p. However, the gamma functions are infinite when their arguments are nonpositive integers. Consequently,

$$\begin{aligned}H_{m,p}(x) &= 0, \qquad m \geqslant p+1, \qquad x<0\\&= 0, \qquad p \geqslant m, \qquad x>0\end{aligned}\tag{5.1}$$

which means that the limits on the inner summations in (4.16) can take the forms listed in table 1.

The density is normalized (figure 1 and equation (2.1)) such that the projected density lies entirely within $|\xi| < a$. Therefore, to be consistent, $\bar{\lambda}_N(r, \theta)$ should be zero for $r > a$. We introduce the terminology:

$$\{\alpha_{m,p}, \beta_{m,p} | m \leqslant 2p, 0 \leqslant p \leqslant L\} \sim \text{set of } \textit{significant} \text{ coefficients}$$

$$\{\alpha_{m,p}, \beta_{m,p} | m \geqslant 2p+1, 0 \leqslant p \leqslant L\} \sim \text{set of } \textit{redundant} \text{ coefficients.}$$

Table 1. Summation limits appearing in equation (4.16)

	$r < a$	$r > a$
M_1^-	0	$p+1$
M_1^+	p	N_1
M_2^-	0	p
M_2^+	$p-1$	N_2

Table 1 and equation (4.16) show that $\bar{\lambda}_N(r, \theta)$ is not consistent if any of the redundant coefficients have appreciable magnitude. So, we introduce the consistency condition:

$$\alpha_{m,p} = \beta_{m,p} = 0, \qquad \forall m, p \in m \geqslant 2p+1, \qquad 0 \leqslant p \leqslant L. \tag{5.2}$$

Measured data are always imperfect so that the consistency condition is bound to be violated in practice. Denote by σ_R and σ_S respectively the standard deviations of the redundant coefficients and the errors in the significant coefficients, due to random errors of standard deviation σ in the given data. The theory of normal matrices for the evaluation of coefficients, as used for instance by Crowther *et al* (1970a), shows that

$$\sigma_R \simeq \sigma_S \simeq \frac{4\sigma}{\pi^2}. \tag{5.3}$$

However large N is the fact that it is finite prevents the reconstruction of some detail in the image. We use the accepted term angular aliasing to denote the cause of this type of image distortion.

Results of a number of computations have suggested to us that angular aliasing does not significantly affect the magnitudes of the redundant coefficients, unless N is small (about 5 or less). Consequently, our present opinion is that $\pi^2\sigma_R/4$ is a meaningful *a posteriori* measure of the error level in the given projections.

Judicious truncation of the series in (4.16) can sometimes improve the signal to noise ratio of the reconstructed image. This is analogous to the standard procedure of enhancing noisy images by low-pass filtering (Rosenfeld 1969). The point is that even if the random errors in the given projections are uniformly (statistically) distributed over the real plane (see figure 1), in the Fourier transform plane the magnitude of the errors tends to increase radially. This is emphasized by the factor ρ multiplying $\Lambda_N(\rho, \phi)$ in (4.2) and by the factors (proportional to p) multiplying the coefficients $\alpha_{m,p}$ and $\beta_{m,p}$ in (4.16).

In our current work we find that even when there actually is density for $r > a$, and the image is reconstructed from projections restricted to $\xi \leqslant a$, then the image obtained from the significant coefficients of the FSI scheme is much less distorted than that obtained from the spread and linear interpolation schemes.

6. Basic image

If $F(\xi, \phi)$ has no angular, trigonometrical Fourier components of order higher than N then the right hand side of (4.5) is an exact representation of $F(\xi, \phi)$. In general, $F(\xi, \phi)$ has higher order Fourier components so that the $A_m(\xi)$ and $B_m(\xi)$ introduced in (4.16) will be subject to aliasing errors (cf Cooley *et al* 1967). Consequently, we can usefully

investigate interpolations $\bar{F}'_N(\xi, \phi)$ of $\bar{F}_N(\xi, \phi)$, where

$$\bar{F}'_N(\xi, \phi) = \bar{F}_N(\xi, \phi) + \Phi(\xi, \phi) S_N(\phi) \tag{6.1}$$

$$|\Phi(\xi, \phi)| < \infty \tag{6.2}$$

$$S_N(\phi_n) = S_N(\phi_n + \pi) = 0, \qquad 1 \leqslant n \leqslant N \tag{6.3}$$

and, because of the foregoing discussion,

$$\Phi(\xi, \phi) = \sum_{q=1}^{I} \{\hat{A}_q(\xi) \cos(q\phi) + \hat{B}_q(\xi) \sin(q\phi)\} \tag{6.4}$$

where the $\hat{A}_q(\xi)$ and $\hat{B}_q(\xi)$ are arbitrary, apart from the very weak constraint (6.2); and I can be any positive integer. However, the condition

$$I = N - 1 \tag{6.5}$$

permits all the Fourier components of $\bar{F}'_N(\xi, \phi)$ to be independent (*a priori*) of those of $\bar{F}_N(\xi, \phi)$. This condition also simplifies the analysis, so that it is used in the following discussion, which is restricted to cases for which the given projections are equally spaced in angle:

$$\phi_n = \frac{n\pi}{N}. \tag{6.6}$$

It is convenient to take

$$S_N(\phi) = 2 \sin(N\phi). \tag{6.7}$$

We write

$$\bar{F}'_N(\xi, \phi) = \sum_{m=0}^{2N-1} \{A'_m(\xi) \cos(m\phi) + B'_m(\xi) \sin(m\phi)\} \tag{6.8}$$

where (4.5) and (6.1) through (6.7) show that

$$A'_0(\xi) = A_0(\xi), \qquad B'_0(\xi) = B_0(\xi) = 0, \tag{6.9}$$

$$A'_m(\xi) = A_m(\xi) + \hat{B}_{N-m}(\xi), \qquad B'_m(\xi) = B_m(\xi) + \hat{A}_{N-m}(\xi), \qquad 1 \leqslant m \leqslant N-1, \tag{6.10}$$

$$A'_N(\xi) = A_N(\xi), \qquad B'_N(\xi) = B_N(\xi) = 0, \tag{6.11}$$

$$A'_m(\xi) = -\hat{B}_{m-N}(\xi), \qquad B'_m(\xi) = \hat{A}_{m-N}(\xi), \qquad N+1 \leqslant m \leqslant 2N-1. \tag{6.12}$$

We now introduce $\{\alpha'_{m,p}, \beta'_{m,p} | 0 \leqslant m \leqslant 2N+1, 0 \leqslant p \leqslant L\}$ the members of which are connected with the members of $\{A'_m(\xi), B'_m(\xi) | 0 \leqslant m \leqslant 2N-1\}$ through (4.7) and (4.8) with the symbols A, B, α and β replaced by A', B', α' and β'. Combining (6.10) and (6.12) leads to

$$\alpha'_{N-q,p} = \alpha_{N-q,p} - \alpha'_{N+q,p}, \qquad 1 \leqslant q \leqslant N-1. \tag{6.13}$$

The $\alpha'_{m,p}$ must satisfy the same consistency condition as the $\alpha_{m,p}$, so that

$$\alpha'_{m,p} = 0, \qquad m \geqslant 2p+1 \tag{6.14}$$

from (5.2). Combining (6.13) and (6.14) gives

$$\alpha'_{m,p} = \alpha_{m,p}, \qquad 0 \leqslant m \leqslant 2N-2p-1 \tag{6.15}$$

which remains true if α is replaced by β. Consequently, we introduce the terminology:

$$\{\alpha_{m,p}, \beta_{m,p} | m \leqslant \min(2p, 2N-2p-1, N), 0 \leqslant p \leqslant N-1\}$$

$$\sim \text{set of unambiguous coefficients.}$$

As shown by (6.15), the unambiguous coefficients derived from the FSI scheme (§4.5) are unchanged as $\Phi(\xi, \phi)$ is varied. This result still holds for $I > N-1$, but the analysis is not given here because it is more complicated and because the result is relatively uninteresting, since we cannot estimate $F(\xi, \phi)$ to higher order than the right hand side of (4.5) when we are only given N projections.

If only the unambiguous coefficients are used to reconstruct the density, so that the summation limits in (4.16) are

$$M_1^- = 0, M_1^+ = \min(p, N-p-1, \tfrac{1}{2}N), M_2^- = 0, M_2^+ = \min(p-1, N-p-1, \tfrac{1}{2}N-1), \quad (6.16)$$

then we say we have a basic image which is free of any artefacts which might be introduced by a particular interpolation scheme, such as any of the ones described in § 4.1 through § 4.4.

Various computations have confirmed that the unambiguous coefficients, for a particular value of N, do not change when more projections are given. The ambiguous members of the set of significant coefficients do change markedly. However, as was mentioned in § 5, the standard deviation of the redundant coefficients computed for a particular number of projections changes very little as the number of given projections increases.

7. Resolution and uncertainty

Given some number N of measured projections one wishes to know what fineness of detail can be attained in the reconstructed image. This is the problem of resolution in which one asks how close two independent features of the image can be before they become indistinguishably merged. It is difficult to find unambiguous answers because the attainable resolution is appreciably affected by the detailed shapes not only of the two features but also of the neighbouring parts of the image.

The density is zero for $|x| > a$ and $|y| > a$ so that, from the sampling theorem, $\omega(x, y)$ is uniquely defined by $\Omega(m/a, n/a)$ where m and n are integers in the range $(-\infty, \infty)$. The given data can only be related directly to the values which $\Omega(\alpha, \beta)$ assumes on straight lines passing through the origin of the Fourier transform plane. So, we cannot compute $\Omega(m/a, n/a)$, for all m and n, from the given data unless, as Crowther *et al* (1970a) do, we take $\Omega(\alpha, \beta) = \Lambda(\rho, \phi)$ to be negligible for ρ greater than some finite value. This means effectively that $\Omega(\alpha, \beta)$ need only be known at a finite number of sample points. Therefore, the required values of $\Omega(\alpha, \beta)$ can be estimated by inverting matrices of finite order.

Since details of the image are unknown before reconstruction, we can only guess the value of ρ beyond which $\Omega(\alpha, \beta)$ is negligible. So, we can only guess the number of sample points needed to reconstruct the image satisfactorily. Because of this we feel that, when the given projections are equally spaced, direct interpolation of the given data is as justifiable a way of calculating the samples needed for the fast Fourier transform algorithm as the methods of Crowther *et al* (1970a).

If we use the FSI scheme (§ 4.5) and reconstruct only the basic image then we know that the computational procedure cannot have introduced misleading artefacts; the standard deviation σ_R of the redundant coefficients indicates the error level due to imperfections in the given data.

An interesting facet of the basic image is that its resolution is not uniform in the sense of Klug and Crowther (1972). If L in (4.16) is restricted to be less than $\frac{1}{2}N$ then $\bar{\lambda}_N(r, \theta)$ is an image with uniform resolution, but it contains only half the unambiguous information contained in the given projections.

Consequently, we feel that, instead of attempting to apply conventional resolution criteria, it is more useful to reconstruct the image from the unambiguous coefficients if one desires to make sure that no artefacts are introduced by the computational procedure. Of course, it must be remembered that our basic image has been derived only for equally spaced projections. We have not found any analysis, similar to that presented in § 6, applicable to unequally spaced projections.

The foregoing reasoning applies only to images about which one has no preknowledge apart from the radii of their circumscribing circles. If one knows *a priori* that the image has some special topology then one can sometimes overcome the limits set by the basic image. For instance, if the image is contained in a rectangle of known size and the rectangle is divided into a known rectangular grid, with the intensity of the image being unknown but constant in each cell of the grid, then the image can be reconstructed from a single projection, as is demonstrated in appendix 1. It is obvious that for all but very specialized (or contrived) classes of image, a single projection gives no information concerning the detailed structure of the image. So, this example of the rectangular image shows that one must be careful not to force unwarranted uniqueness on a reconstruction method by making computationally convenient assumptions concerning the topological structure of the image. Gilbert's (1972b) discussion of the ART technique (Gordon *et al* 1970, Herman and Rowland 1971) reinforces this point.

Another question which can be discussed quantitatively is how much uncertainty (or what error level) is introduced into the image by only N projections being given. The rho-filtered discrete layergram (§ 4.2), which is the accurate image in the limit of an infinite number of projections, is also translationally invariant with respect to the given data so that the reconstruction of a particular feature can be considered independently of the rest of the image.

We take a smooth 'blob' of density centred at the point (r_0, θ_0) of the r, θ plane (figure 1(*a*)). We find it convenient to give the blob a 'gaussian' shape:

$$\exp[-\{r^2 + r_0^2 - 2rr_0 \cos(\theta - \theta_0)\}/2w^2],$$

where w is the effective width of the blob. We then calculate the N projections of this density when ϕ_n and $S_N(\phi)$ are given by (6.6) and (6.7) respectively. In appendix 2 it is shown that the rho-filtered discrete layergram computed from these projections can be expressed as the sum of the original blob plus 'clutter' spread over the r, θ plane.

The clutter is a function of w, N and the distance from (r_0, θ_0). Since the relative positions of features of an image are unknown *a priori*, the clutter must be looked upon as noise on the true image. The image degradation is greatest where the noise level is largest. Accordingly, in figure 2 we present a plot of the maximum magnitude of the clutter associated with the gaussian blob (itself having a maximum magnitude of unity) as a function of r/w and N. Thus, figure 2 permits one to estimate the noise level present in an image due to a feature of a particular size and intensity when N projections are

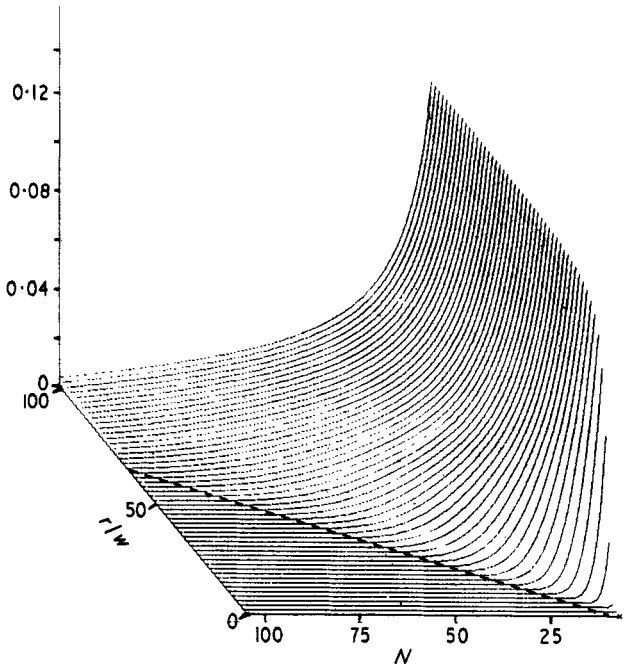

Figure 2. Maximum magnitude of clutter associated with gaussian blob as a function of r/w and N.

given. At points in the image, the clutter associated with a number of features may add constructively and give a misleading artefact. An important aspect of the basic image is that it is a smooth approximation to the true image.

An interesting point is that if the number of projections satisfies the resolution criterion advanced by Crowther *et al* (1970a) then the clutter exhibited by the rho-filtered layergram is of similar level to that exhibited by the other interpolation schemes (for the gaussian blob, the clutter level lies to the left of the dashed line in figure 2).

8. Computational results

We now present some computational examples to reinforce points made in previous sections.

We first use ideal data (the 'given' projections are computed, not measured). We consider circular cylinders offset from the centre of the real plane. The abrupt changes of density at the edges of the cylinders represent crucial tests for the computational procedures. We also present images reconstructed from measured projections of a bovine shin bone (tibia and fibula). In all of these examples the images are reconstructed from 20 equally spaced projections and are computed on a square 128 by 128 point grid.

We first illustrate the 'smoothness' of the basic image. Figure 3 shows the ideal image of a solid cylinder, its basic image and its image obtained from the FSI interpolation scheme. The FSI image is sharper than the basic image but it exhibits much sharply peaked clutter.

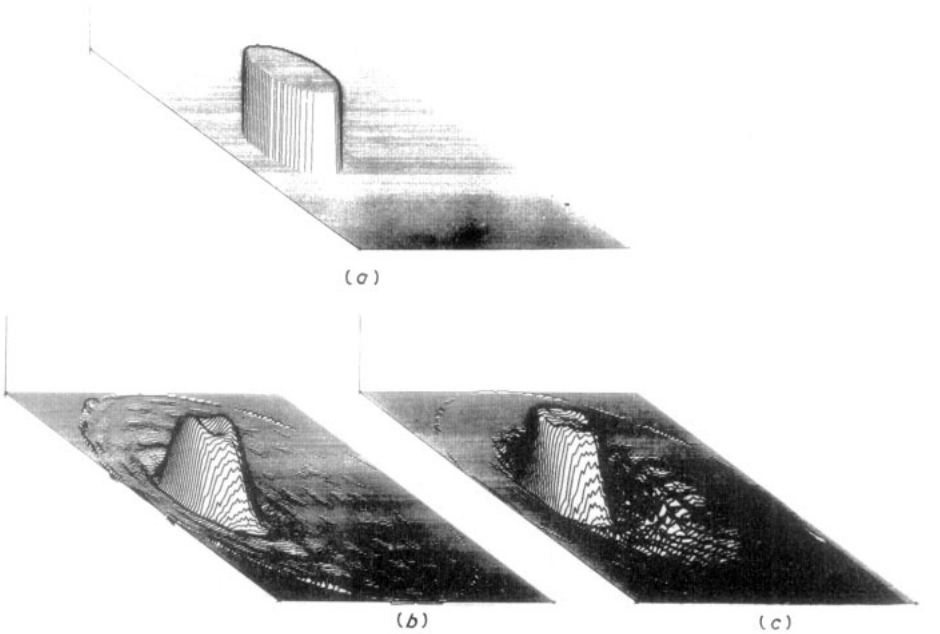

Figure 3. Images of off-centred circular disc. In these perspective images the apparent height is proportional to density. (*a*) Ideal image, (*b*) basic image and (*c*) FSI image.

We now compare the interpolation schemes introduced in § 4. Figure 4 shows contour plots of images of a hollow cylinder. The reconstructed images for the FSI, linear and spread interpolation schemes exhibit few significant differences and their clutter levels are similar. The rho-filtered discrete layergram (figure 4(*e*)) has more clearly defined edges but its clutter level is twice as large as that of the three previous images. The discrete layergram (figure 4(*f*)) is a heavily blurred image; the cylinder edges are not defined and it is not obvious that the density is less at the centre of the cylinder. Since the images shown in figures 4(*c*) and 4(*d*) require significantly less computer time than the image shown in figure 4(*b*), one can conclude that either the linear or spread interpolation schemes should be used when it is advantageous to conserve computer time.

We obtained x ray photographs of a bovine shin bone and an aluminium step wedge (as a calibration control) using standard clinical radiographic apparatus. We obtained the required projections of a particular cross section of the bone by scanning the photographs with a microdensitometer, which permitted us to correct for film nonlinearities. We cut out a thin slice of the bone containing the cross section which we examined. An x ray photograph of this slice is shown in figure 5 (plate). The images in figure 6 were computed and were made by successive character overprints on the standard lineprinter used in the Computer Centre of the University of Canterbury. This method of making images has been described by MacLeod (1970). The discrete layergram (figure 6(*a*)), which is what would be obtained (ideally) from a conventional transverse tomograph, is seen to be very heavily blurred, and it is not clear that there is a hole in the middle of it. The rho-filtered discrete layergram (figure 6(*b*)) has a high clutter level but it displays all the main features of figure 5 (plate). It is clear that medical tomography

Figure 5. Actual bovine shin bone cross section.

[*facing page* 374]

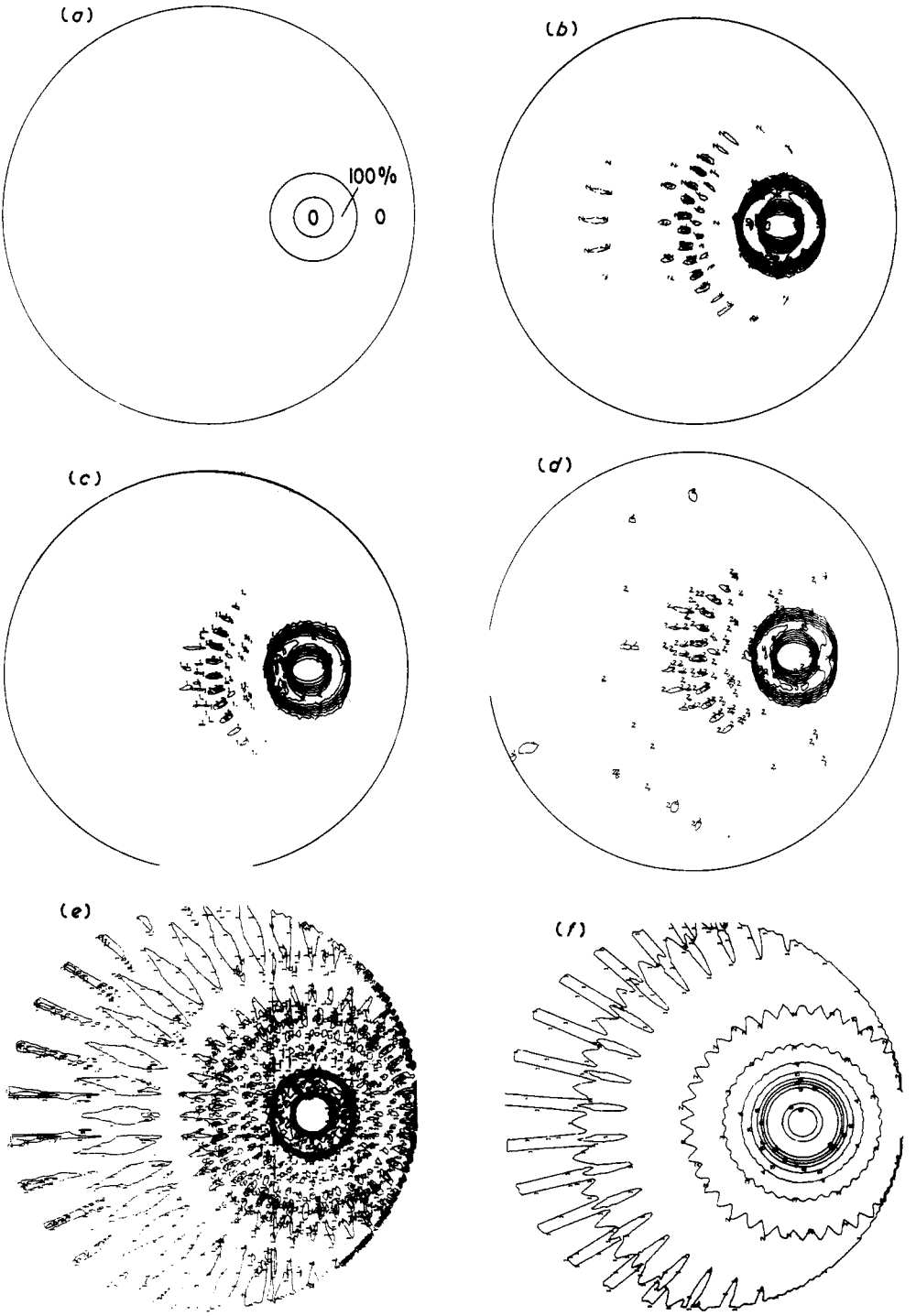

Figure 4. Results of interpolation schemes on ideal data. (*a*) Ideal object, (*b*) Fourier series interpolation (FSI), (*c*) linear interpolation, (*d*) spread interpolation, (*e*) rho-filtered discrete layergram and (*f*) discrete layergram. Images are contoured in steps corresponding to 10% of the maximum density.

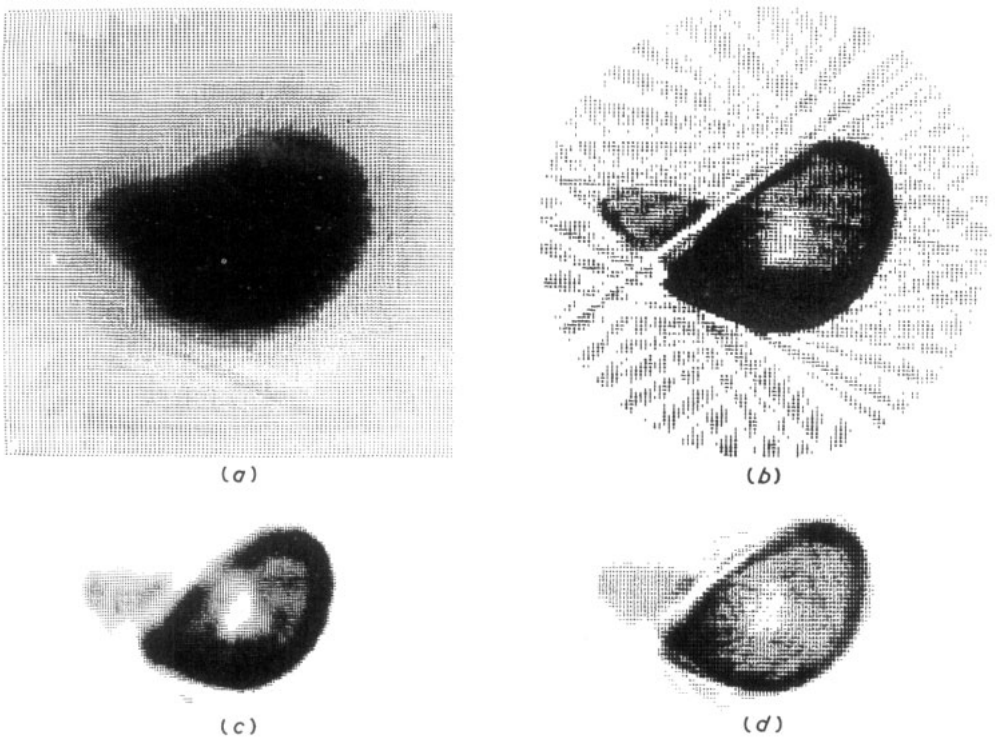

Figure 6. Reconstructions of bovine shin bone cross section from real data. (*a*) Discrete layergram of bone, (*b*) rho-filtered discrete layergram of bone, (*c*) basic image of bone and (*d*) linear, spread and FSI reconstruction of bone.

would be improved if rho-filtered discrete layergrams, rather than plain discrete layergrams, could be displayed, as we have previously suggested (Bates and Peters 1971). Figure 6(*c*) shows the basic image, which is less contaminated with clutter than the rho-filtered discrete layergram. The linear, spread and FSI interpolation schemes all lead to similar images. The image shown in figure 6(*d*), which was got from the spread scheme, is clearly an improvement on the basic image; and it also contains no misleading artefacts because the 20 given projections are sufficient for reconstructing the significant detail in the image. It must be remembered, however, that it will often not be possible to estimate *a priori* how many projections are necessary to prevent the appearance of artefacts.

To illustrate the procedure developed in appendix 1, whereby an image with a certain topology can be reconstructed from a single projection, we computed a rectangular grid image of the bone with the density being constant in each cell of the grid. We then used this image to compute the pseudoprojection which would be measured if the actual cross section of the bone had this contrived form. The pseudoprojection is shown in figure 7(*a*) and the reconstructed image (by the method of appendix 1) in figure 7(*b*), which is very similar to figure 5 (plate). Shown in figure 7(*c*) is an actual measured projection. The image, reconstructed from it by the method of appendix 1, is shown in figure 7(*d*). It bears no relation to figure 5 (plate) as is of course expected, since for cross sections with topologies which occur in practice there is a continuous infinity of images corresponding to a single projection.

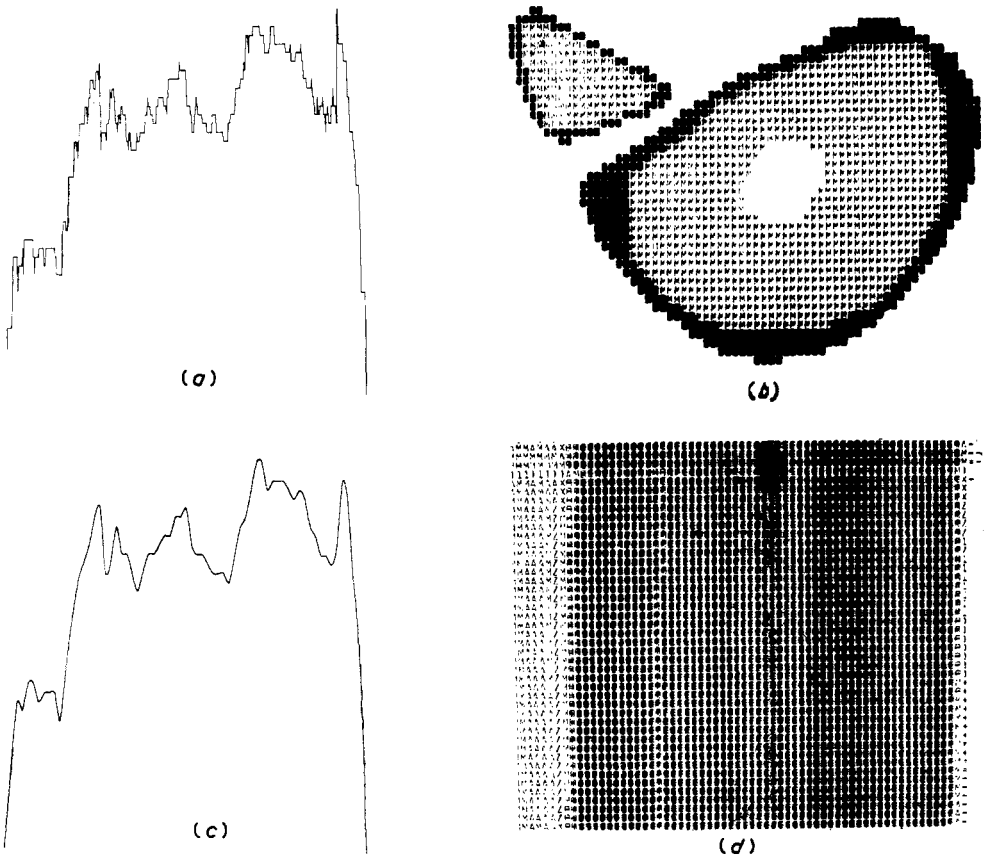

Figure 7. Reconstruction from a single projection. (*a*) Pseudoprojection of bone, (*b*) actual digitized cross section and reconstruction from pseudoprojection in (*a*), (*c*) actual projection of bone and (*d*) reconstruction from projection in (*c*).

9. Conclusions

In scientific work there are two main reasons for reconstructing images of objects. Firstly, one may wish to inspect the image to see if it contains any unsuspected feature (after all, this is one way discoveries happen). Secondly, one may wish to learn if certain known features are present in the image.

When concerned with the first of these reasons, especially when one is not completely certain that the density is restricted to $r \leqslant a$, one should compute the basic image; it is free of artefacts (one will not make unwarranted discoveries!). Also, one can estimate the accuracy of the image *a posteriori*.

The second reason is most likely to apply in more routine situations when many images need to be reconstructed, so that computational economy is important. In such cases, especially when one is certain that the density is zero for $r > a$, one should use a simple interpolation scheme. The results presented in § 8 indicate that rho-filtered discrete layergrams exhibit appreciably more clutter than images got from the interpolation schemes described in §§ 4.3, 4.4 and 4.5, all three of which give comparable

results. The computer times required for spread interpolation (§ 4.3) and linear interpolation (§ 4.4) are about the same (see table 2) and are both much shorter than the time required for the FSI scheme (§ 4.5). Because linear interpolation is smoother, it should probably be preferred to spread interpolation.

Table 2. Computer times for several reconstruction methods†

Method	Time to reconstruct 20 128-point scans on a 128×128 point grid (min)	Approximate time to reconstruct N M-point scans on an $M \times M$ point grid $\times 10^{-5}$ (min)
Layergram	1·9	$0{\cdot}6M^2N$
Rho-filtered layergram (using FFT)	2·2	$(0{\cdot}6M + 1{\cdot}6 \log_2 M)MN$
Spread/linear interpolation (using FFT)	0·8	$\{2M + 6N + (0{\cdot}15M + 0{\cdot}8N) \log_2 M\}M$
Fourier series interpolation	2·9	$0{\cdot}9M^2N$
CON (direct convolution, Ramachandran and Lakshminarayanan 1971)	2·5	$0{\cdot}76M^2N$
ART (algebraic reconstruction technique, Gordon *et al* 1970)	$\geqslant 4$	$1{\cdot}25M^2NI$‡
Conventional Fourier transform (computing the linear interpolation scheme and using trapezoidal integration rule to evaluate Fourier integrals)	1160§	$(43M^2 + 2)M^2$

† Excluding overheads in the form of disc transfer operations, data input/output etc.
‡ I is the number of iterations required for convergence. Its value depends on the type of data used (cf Gilbert 1972*a*).
§ This time was obtained by extrapolating from the reconstruction time of a smaller problem.

Klug and Crowther (1972) point out that the resolution criterion (that if the resolution distance, in an image of maximum diameter $2a$, is to be d then the necessary number of projections is $2\pi a/d$) originally advanced by Crowther *et al* (1970a) leads to an image which is both free of artefacts and uniformly resolved. They also indicate that an image, having twice the resolution at its centre as it has at its periphery, can be free of angular aliasing errors. Such an image can only be built up from a restricted number of the eigenfunctions considered by Klug and Crowther (1972). Their figure 3, which shows the restrictions on their radial and angular eigenfunctions, is reminiscent of the restrictions on m and p given in § 6 for the unambiguous coefficients. Consequently, our basic image is similar to Klug and Crowther's aliasing-free image. The improvements that we introduce here are, first that our consistency condition permits *a posteriori* assessment of the quality of the given data, and second that we prove that our basic image contains only that information common to all physically permissible interpolations of the given projections (provided that they are equally spaced in angle).

Finally, we discuss computational economy. We emphasize the speed of the fast Fourier transform (FFT) algorithm (Cooley and Tukey 1965, Bergland 1969). Comments

made by some authors (cf Ramachandran and Lakshminarayanan 1971 and Gilbert 1972a) suggest that they do not realize that this algorithm is necessarily faster (even if, for algorithms based on 'direct' methods, tabulations of special functions are prestored in the computer memory) when handling multitudes of data, because it reduces the number of computational operations. If N Fourier components are to be computed, the time required for the FFT algorithm is proportional to $N\log_2 N$, compared with N^2 for a conventional Fourier transform algorithm. Table 2 compares the time required for the schemes described in this paper and for two 'direct' methods. The last item in table 2 emphasizes the importance of the FFT algorithm and explains perhaps why those who have not yet appreciated its niceties tend to avoid computing Fourier transforms. The times given in the second column of table 2 were got by running all the methods on the same computer (IBM 360/44 at the Computer Centre, University of Canterbury).

Acknowledgments

We acknowledge the assistance given to us by Dr R D Gibson of the X ray Department, Christchurch Hospital in producing radiographs suitable for use as data. Many helpful comments and pertinent references to the literature have come from R A Crowther, P F C Gilbert and A Klug of the MRC Laboratories, Cambridge, and P T Gough and C L Miles of the University of Canterbury. Two of us acknowledge financial support in the forms of a NZUGC postgraduate scholarship (TMP) and a University of Canterbury Postdoctoral Fellowship (PRS).

Appendix 1

Consider a rectangular image, of dimensions A by B, divided into $M_x M_y$ rectangular cells, where M_x and M_y are positive integers. Figure 8 shows the geometry. The density is constant within each cell.

$$\omega(x, y) = \omega_{m,n}, \qquad m \leqslant x + \tfrac{1}{2}M_x + 1 < m+1,$$
$$n \leqslant \tfrac{1}{2}M_y - y + 1 < n+1, \qquad 1 \leqslant m \leqslant M_x, \qquad 1 \leqslant n \leqslant M_y. \qquad \text{(A.1)}$$

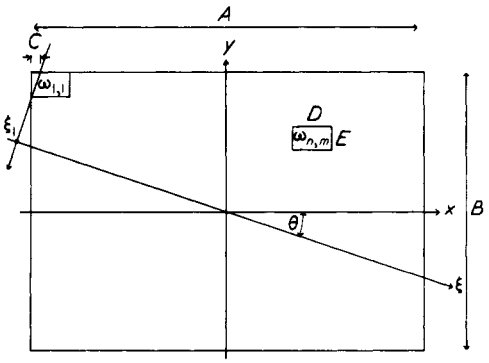

Figure 8. Geometry of grid for constructing pseudoprojection. A, B overall dimensions of grid, C spacing on x axis between adjacent projection samples = $A/(M_x M_y)$. D, E cell dimensions.

We project the image on to the ξ axis which is oriented at an angle to the x axis of θ, which is given in terms of the integer M_y by

$$\theta = \tan^{-1}\left(\frac{1}{M_y}\right). \tag{A.2}$$

The resulting pseudoprojection is then sampled at points ξ_k, where

$$\xi_{k-1} - \xi_k = \frac{A}{M_x M_y \cos\theta}, \tag{A.3}$$

$$\xi_1 = -\tfrac{1}{2}\left\{A \sec\theta + \left(B - A\tan\theta - \frac{2B}{M_y}\right)\sin\theta\right\} \tag{A.4}$$

as shown in figure 8. $f(\xi_k, \theta)$ is then given by

$$f(\xi_k, \theta) = \alpha\left(\sum_{i=l+1}^{M_y} \delta_m \omega_{i,m} + \sum_{i=1}^{l} \omega_{i,m+1}\right), \tag{A.5}$$

$$l = k(\text{mod } M_y),$$

$$m = \frac{k-l}{M_y}$$

$$\delta_m = 0, \qquad m = 0$$

$$= 1, \qquad m \neq 0$$

$$\alpha = \frac{B \sec\theta}{M_y}.$$

α is a constant of proportionality made necessary by the path of integration through each cell. If one is given the $M_x M_y$ values of $f(\xi_n, \theta)$, then each member of $\{\omega_{m,n}\}$ can be obtained iteratively starting with

$$\omega_{1,1} = \alpha f_1 \tag{A.6}$$

which can be substituted into (A.5) to give $\omega_{1,2}$. This process may be continued until eventually all the $\omega_{m,n}$ are obtained. Note that the given data is equivalent to a single projection given at $M_x M_y$ values of ξ.

Appendix 2

Because rho-filtered discrete layergrams are linear in the given data, the clutter (due to N being finite) associated with a particular feature is a function only of the radius vector from an appropriately chosen origin in the feature. Consequently, when analysing the gaussian blob introduced in § 7, it is sufficient to centre the blob at the origin of coordinates of figure 1(*a*). Thus,

$$\lambda(r, \theta) = \exp\left(\frac{-r^2}{2w^2}\right) \tag{A.7}$$

of which the projected density is

$$f(\xi, \phi) = (2\pi)^{1/2} w \exp\left(\frac{-\xi^2}{2w^2}\right) \tag{A.8}$$

which gives, using (2.6) and formula 11.4.29 of Abramowitz and Stegun (1965),

$$\Lambda(\rho, \phi) = 2\pi w^2 \exp(-2\pi^2 w^2 \rho^2). \tag{A.9}$$

From (3.4) and (4.2) the rho-filtered layergram is

$$\bar{\lambda}_N(r, \theta) = \frac{4\pi^2 w^2}{N} \sum_{n=1}^{2N} \int_0^\infty \int_0^{2\pi} \delta\left\{\phi - \left(\frac{n\pi}{N}\right)\right\} \times \exp(-2\pi^2 w^2 \rho^2) \exp\{-i2\pi r\rho \cos(\phi - \theta)\}\rho \, d\phi \, d\rho \tag{A.10}$$

when ϕ_n is given by (6.6). Expressing the complex exponential in (A.10) as a trigonometrical Fourier series (cf formulae 9.1.44 and 9.1.45 of Abramowitz and Stegun 1965), integrating with respect to ϕ, summing over n and writing $t = 2^{1/2}\pi w\rho$ gives

$$\bar{\lambda}_N(r, \theta) = 4 \sum_{m=0}^{\infty} \epsilon_m (-1)^{mN} \cos(2mN\theta) \int_0^\infty J_{2mN}\left(\frac{2^{1/2} rt}{w}\right) \exp(-t^2) t \, dt \tag{A.11}$$

where ϵ_m is the usual Neumann factor. The term for $m = 0$ in (A.11) is $\lambda(r, \theta)$, as given by (A.7). The remaining terms can be evaluated by integrating by parts, which replaces $tJ_{2mN}(2^{1/2}rt/w)$ in the integrand by a constant multiplied to the derivative of the Bessel function, and then using the second recurrence relation in formula 9.1.27 of Abramowitz and Stegun (1965). The resulting integrals can be expressed in terms of modified Bessel functions using equation (5), p 394, of Watson (1966). So, the clutter introduced by there being only N given projections can be written as

$$\bar{\lambda}_N(r, \theta) - \lambda(r, \theta) = \frac{\pi^{1/2} r}{2^{1/2} w} \exp\left(\frac{-r^2}{4w^2}\right) \sum_{m=1}^{\infty} \left\{I_{mN-1/2}\left(\frac{r^2}{4w^2}\right) - I_{mN+1/2}\left(\frac{r^2}{4w^2}\right)\right\} \cos(2mN\theta). \tag{A.12}$$

References

Abramowitz M and Stegun I A 1965 *Handbook of Mathematical Functions* (New York: Dover)
Bates R H T and Napier P J 1972 *Mon. Not. R. Astronom. Soc.* **158** 405–24
Bates R H T and Peters T M 1971 *N.Z. J. Sci.* **14** 883–96
Bellman S H, Bender R, Gordon R and Rowe J E 1971 *J. theor. Biol.* **32** 205–16
Bergland G D 1969 *IEEE Spectrum* **6** 41–52
Bracewell R N 1956 *Aust. J. Phys.* **9** 198–217
—— 1961 *IRE Trans.* **AP-9** 59–67
Bracewell R N and Riddle A C 1967 *Astrophys. J.* **150** 427–34
Cooley J W , Lewis P and Welch P 1967 *IEEE Trans.* **AU-15** 79–84
Cooley J W and Tukey J W 1965 *Math. Comp.* **19** 297–301
Cormack A M 1963 *J. appl. Phys.* **34** 2722–7
—— 1964 *J. appl. Phys.* **35** 2908–12
Crowther R A , DeRosier D J and Klug A 1970a *Proc. R. Soc.* A **317** 319–40
Crowther R A *et al* 1970b *Nature, Lond.* **226** 421–5
Crowther R A and Klug A 1971 *J. theor. Biol.* **32** 199–203
DeRosier D J and Klug A 1968 *Nature, Lond.* **217** 130–4
Gilbert P F C 1972a *Proc. R. Soc.* B **182** 89–102
—— 1972b *J. theor. Biol.* **36** 105–17
Goodman J W 1968 *Introduction to Fourier Optics* (New York: McGraw-Hill)
Gordon R, Bender R and Herman G T 1970 *J. theor. Biol.* **29** 471–81
Herman G T and Rowland S 1971 *J. theor. Biol.* **33** 213–23
Hildebrand F B 1956 *Introduction to Numerical Analysis* (New York: McGraw-Hill)
Kishi K, Kurihara S, Yuasa M and Gouke H 1969 *Toshiba Rev.* **43** 36–41

Klug A and Crowther R A 1972 *Nature, Lond.* **238** 435–40
Kotoulas K and Sinis G 1970 *Röntgenblatter* **23** 15–9
MacLeod I D G 1970 *IEEE Trans.* **C-19** 160–2
Ramachandran G N and Lakshminarayanan A V 1971 *Proc. Natn. Acad. Sci. USA* **68** 2236–40
Rosenfeld A 1969 *Picture Processing by Computer* (New York: Academic Press)
Schneeman J G 1968 *Industrial X-ray Interpretation* (Evanston, Ill.: Intex)
Skolnik M 1962 *Introduction to Radar Systems* (New York: McGraw-Hill)
Stanton L 1969 *Basic Medical Radiation Physics* (New York: Meridith)
Swenson G W and Mathur N C 1968 *Proc IEEE* **56** 2114–30
Vainshtein B K 1971 *Sov. Phys.–Crystallogr.* **15** 781–7
Vogt F B, Meharg L S and Mack P B 1969 *Am. J. Roentg.* **105** 870–6
Watson G N 1966 *Bessel Functions* (London: Cambridge University Press)